samples D1, D2, and D3. For sample D1, the onset of the simulated imaginary permeability peak occurs at ~1.15 THz, which corresponds well with the onset of the experimental peak in $\tan^{-2}(\Psi)$. The noticeable difference in the actual peak locations is to be expected, because $\tan^{-2}(\Psi)$ consists of ratios of absolute values; i.e., the resonance width observed is dependent on the strength of the oscillator. Thus, it is important when considering $\tan^{-2}(\Psi)$ and $\mu_{eff}(\omega)$ to compare the onset of the resonances.

The scalability of these magnetic metamaterials throughout the THz range and potentially into optical frequencies promises many applications, such as biological (*19*) and security imaging, biomolecular fingerprinting, remote sensing, and guidance in zero-visibility weather conditions. Additionally, the effect is nearly an order of magnitude larger than that obtained from natural magnetic materials (*20*). Structures with a negative magnetic response, when combined with plasmonic wires that exhibit negative electrical permittivity (*21*–*24*), should produce a negative refractive index material at these very high frequencies, enabling the realization of needed devices in the THz regime.

References and Notes

1. R. Ulrich, *Infrared Phys.* **7**, 37 (1967).
2. S. T. Chase, R. D. Joseph, *Appl. Opt.* **22**, 1775 (1983).
3. R. A. Shelby, D. R. Smith, S. Schultz, *Science* **292**, 79 (2001).
4. J. B. Pendry, A. J. Holden, D. J. Robbins, W. J. Stewart, *IEEE Trans. Microw. Theory Tech.* **47**, 2075 (1999).
5. P. Grunberg, F. Metawe, *Phys. Rev. Lett.* **39**, 1561 (1977).
6. J. R. Sandercock, W. Wettling, *J. Appl. Phys.* **50**, 7784 (1979).
7. R. E. Camley, M. Grimsditch, *Phys. Rev. B* **22**, 5420 (1980).
8. R. E. Camley, D. L. Mills, *Phys. Rev. B* **26**, 1280 (1982).
9. L. Remer, B. Luthi, H. Sauer, R. Geick, R. E. Camley, *Phys. Rev. Lett.* **56**, 2752 (1986).
10. M. R. F. Jensen, S. A. Feiven, T. J. Parker, R. E. Camley, *Phys. Rev. B* **55**, 2745 (1997).
11. C. Sirtori, *Nature* **417**, 132 (2002).
12. I. S. Schelkunoff, H. T. Friis, in *Antennas: Theory and Practice*, S. Sokolnikoff, Ed. (Wiley, New York, 1952), p. 584.
13. D. R. Smith, W. J. Padilla, D. C. Vier, S. C. Nemat-Nasser, S. Schultz, *Phys. Rev. Lett.* **84**, 4184 (2000).
14. C. G. Parazzoli, R. B. Greegor, K. Li, B. E. C. Koltenbah, M. Tanielian, *Phys. Rev. Lett.* **90**, 107401 (2003).
15. S. O'Brien, J. B. Pendry, *J. Phys. Cond. Matter* **14**, 6383 (2002).
16. Materials and methods are available as supporting material on *Science* Online.
17. SRRs also have an electric response in both the P- and S-polarized measurements. This electric contribution is about the same for both polarizations, thus a further advantage of the reflectance ratio measurements is that the electric response is minimized.
18. For ease of calculation and maximum magnetic response, the propagation of the incident radiation was parallel to the plane of the SRRs (90° to the surface normal of Fig. 1). The electrical conductivity used for the copper elements was $\sigma = 5.8 \times 10^7$ S/m; for the quartz substrate, we used a dielectric constant of 3.78. The normal component of effective magnetic permeability $\mu_{eff}(\omega)$ can be extracted from the S-parameter simulation results (*25*) and used to calculate the expected theoretical reflectance ratio $\tan^{-2}(\Psi)$ (Fig. 2, bottom) (*26*).
19. X. C. Zhang, *Phys. Med. Biol.* **47**, 3667 (2002).
20. The individual S- and P-polarization data were fit with the standard Lorentzian form for a resonance. The oscillator strength S can be extracted from the fits, and we found values around $S = 0.6$. This is a large effect in comparison with values we calculated from natural magnetic materials, such as FeF_2, which has a value of $S = 0.07$.
21. D. Wu *et al.*, *Appl. Phys. Lett.* **83**, 201 (2003).
22. S. Gupta, G. Tuttle, M. Sigalas, K. M. Ho, *Appl. Phys. Lett.* **71**, 2412 (1997).
23. J. B. Pendry, A. J. Holden, W. J. Stewart, I. Youngs, *Phys. Rev. Lett.* **76**, 4773 (1996).
24. J. B. Pendry, A. J. Holden, D. J. Robbins, W. J. Stewart, *J. Phys. Cond. Matt.* **10**, 4785 (1998).
25. D. R. Smith, S. Schultz, P. Markoš, C. M. Soukoulis, *Phys. Rev. B* **65**, 195104 (2002).
26. D. Schurig, D. R. Smith, in preparation.

27. We thank Dr. S. Wang for his valuable assistance in analyzing Fourier transform infrared spectra. Supported by the Multidisciplinary University Research Initiative of the U.S. Office of Naval Research/Defense Advanced Research Projects Agency (DARPA) (grant no. N00014-01-1-0803), NSF (grant no. DMI 0216423), and the U.S. Army Research Office/DARPA (grant no. ARO DAAD19-00-1-0525).

Supporting Online Material

www.sciencemag.org/cgi/content/full/303/5663/1494/DC1
Materials and Methods
Figs. S1 and S2

25 November 2003; accepted 5 February 2004

Discovery of Ancient Silicate Stardust in a Meteorite

Ann N. Nguyen* and Ernst Zinner

We have discovered nine presolar silicate grains from the carbonaceous chondrite Acfer 094. Their anomalous oxygen isotopic compositions indicate formation in the atmospheres of evolved stars. Two grains are identified as pyroxene, two as olivine, one as a glass with embedded metal and sulfides (GEMS), and one as an Al-rich silicate. One grain is enriched in ^{26}Mg, which is attributed to the radioactive decay of ^{26}Al and provides information about mixing processes in the parent star. This discovery opens new means for studying stellar processes and conditions in various solar system environments.

Presolar grains were isolated in primitive meteorites only 15 years ago. These grains of stardust formed in the atmospheres of evolved stars and in nova and supernova ejecta. They survived processing in the interstellar medium and in the solar nebula, where most material was heated and homogenized to an average composition. Having undergone minimal alteration, they preserve the original isotopic composition of their parent stars and thus provide important information about stellar evolution and nucleosynthesis. The types of presolar grains identified to date include nanodiamonds; silicon carbide; graphite; silicon nitride; and the oxide grains corundum, spinel, and hibonite (*1*). However, spectroscopic data of young main sequence stars (*2*, *3*) and oxygen-rich asymptotic giant branch stars (AGB) (*4*, *5*) indicate an abundance of submicrometer amorphous silicate grains and crystalline silicate grains of forsterite, enstatite, and diopside. Surprisingly, circumstellar silicate grains were absent from the collection of identified presolar grains despite attempts to isolate them from meteorites (*6*–*8*). The question was whether or not these particles were destroyed by processing in the interstellar medium, solar nebula, or the parent body. A major difficulty in identifying anomalous silicate grains is that the solar system formed under oxidizing conditions and, thus, solar system minerals are dominated by oxidized phases such as oxides and silicates. Consequentially, the identification of a few isotopically anomalous O-rich grains in this great sandbox of oxidized phases of solar system composition requires the analysis of a large number of grains. This difficulty is heightened by the limiting spatial resolution (>1 μm) of the instruments used in previous searches and the expected submicrometer sizes of presolar silicates. Here, we analyzed grains ~100 to 500 nm in size from the primitive meteorite Acfer 094 (*9*) by multidetection raster imaging on the Cameca NanoSIMS, a new type of ion microprobe that affords analysis of submicrometer grains (*9*).

We avoided use of any harsh chemical treatments that may destroy silicate grains and, to reduce the background signal from silicates of solar composition, we only analyzed grains from the matrix, making sure not to break apart any inclusions (*9*). These size-separated grains were dispensed from suspension onto a gold substrate to form a tightly packed layer of grains. Isotopic measurements were performed by obtaining negative secondary ion images of the three O isotopes (^{16}O, ^{17}O, and ^{18}O), ^{24}Mg^{16}O, and ^{28}Si, which were simultaneously detected along with secondary electrons (*9*). These ion images not only allow for the identification of grains with anomalous O isotopic ratios, they also enable the identification of silicate grains using the correlated ^{24}Mg^{16}O and ^{28}Si signals. Because the majority of the grains are of solar system origin and called normal grains hereafter, we used them as standards. A candidate grain was considered presolar if its composition fell well outside of the range for normal grains in the image.

After candidate presolar grains were identified by their oxygen isotopic compositions, we relo-

Laboratory for Space Sciences and the Physics Department, Washington University, St. Louis, MO 63130, USA.

*To whom correspondence should be addressed. E-mail: nguyen@wustl.edu

cated them in a field emission–scanning electron microscope (FE-SEM) and obtained images and energy dispersive x-ray (EDX) spectra. To restrict analysis as much as possible to the presolar grains, we used an electron beam of 5 keV. Although the grains had not been completely sputtered away in the ion probe, any distinct surface morphologies may have been destroyed. The sample mount was then taken back to the NanoSIMS, where we succeeded in relocating one anomalous grain in positive secondary ion images of the three Mg isotopes, ^{27}Al, and ^{28}Si (*9*).

In the 16 analyzed 400 μm^2 areas, we identified 9 anomalous grains that are distinct in their oxygen isotopic ratios (Table 1 and Figs. 1 and 2). All of them have ^{24}Mg^{16}O/^{16}O and ^{28}Si/^{16}O ratios within the range for normal matrix grains, which are primarily silicates. The anomalous grain #1 (Table 1, Fig. 1) has an enrichment in ^{17}O and a depletion in ^{18}O. The ^{24}Mg^{16}O and ^{28}Si images indicate that this grain is a Mg-rich silicate. Analysis of its Mg isotopic composition found it to be enriched in ^{26}Mg by 119 ± 15 per mil (‰). All anomalous isotopic ratios should be taken as lower limits because ion imaging of very small, tightly packed grains leads to dilution of any anomalies due to contributions from the surrounding normal grains (*10*).

Messenger *et al.* (*11*) identified six presolar silicates in interplanetary dust particles (IDPs), and recently nine more silicate grains have been added (*12*). Among these grains, one forsterite and two GEMS (glass with embedded metal and sulfides) (*13*) as well as four pyroxenes have been identified. Mostefaoui *et al.* (*14*) located two grains with anomalous O isotopic compositions in the ordinary chondrites Semarkona and Bishunpur. Although the negative secondary ion images indicated the presence of Si, no independent identification of the mineralogy of these grains has been made. More recently, Mostefaoui *et al.* (*15*) located another anomalous grain in Bishunpur and proposed a GEMS composition for this grain. We identified nine presolar grains from a carbonaceous chondrite that we estimate to be silicate grains. The ^{28}Si ion images indicate that all nine grains are Si-rich. To determine the silicate mineral type and the chemical composition of the anomalous grains, we took EDX spectra of six grains (Fig. 3, Table 1; table S1). The EDX spectra indicate that two of the grains are olivines, one is an orthopyroxene, one is a clinopyroxene containing 5 atom % of Ca, and one is an Al-rich silicate. The sixth grain has a high Fe concentration and excess O, making it a candidate for a GEMS. The ^{28}Si/^{16}O ratios of these six silicate grains, as determined from the NanoSIMS, encompass those of the three grains that were not analyzed by EDX. This confirms the silicate nature of these three grains.

Among the grains analyzed by EDX, four have an Fe content greater than the Mg content, but because of the small grain size there are uncertainties in the EDX analysis (*9*). Spectroscopic observations of O-rich dust shells around evolved stars reveal features consistent with abundant amorphous silicates, 90% of which have the composition of olivine, and moderate concentrations of crystalline enstatite, forsterite, and diopside (*5*). For most sources, crystalline enstatite is more abundant than crystalline olivine by a factor of 3 to 4 (*16*). Crystalline silicates are predicted to contain <10 weight % Fe, with amorphous silicates containing more Fe (*5*, *17*). The high Fe content of four of our grains is thus surprising. It could be an experimental artefact where contributing signal is derived from surrounding or underlying grains. In contrast, secondary processes in the solar nebula or on the parent body that introduced Fe into the original forsterite may account for the Fe, considering the small size of these grains. Fe-rich rims around forsterite are abundant in many meteorites (*9*, *18*, *19*).

The abundance of presolar silicates among 100- to 500-nm grains was determined by dividing the total area of presolar grains (~0.66 μm^2) by the total area of all grains analyzed (~5750 μm^2), and then correcting for the detection efficiency of grains in this size range (*9*). We arrive at an abundance of ~230 ppm (parts per million) for this size fraction. The abun-

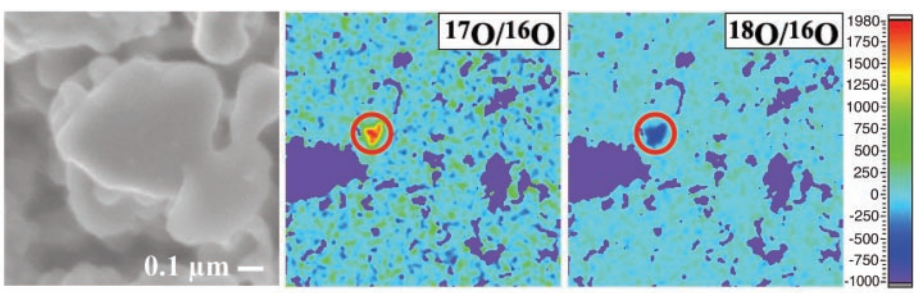

Fig. 1. Oxygen isotopic ratio images of a 100 μm^2 area containing presolar grain #1 (circled). The color bar gives the ratios as delta values (δ) or deviations from solar oxygen isotopic ratios in per mil (‰). Small deviations from normal isotopic composition are due to statistical fluctuations. However, the presolar grain has a much larger anomaly. Ion images of ^{24}Mg^{16}O and ^{28}Si indicate that this is a Mg-rich silicate grain. Also shown is a high-magnification SEM image (top left) of the presolar grain. The EDX spectrum shown in Fig. 3 identifies it as a pyroxene grain.

Table 1. Oxygen isotopic ratios, grain size, and preliminary mineralogical identification of presolar silicate grains from Acfer 094. Un, unidentified.

Number	^{17}O/^{16}O (1σ × 10^{-5})	^{18}O/^{16}O (1σ × 10^{-5})	Diameter (nm)	Mineralogy
1	1.0910 × 10^{-3} (5.31)	7.0043 × 10^{-4} (4.40)	500	Clinopyroxene
2	5.8157 × 10^{-4} (3.65)	2.0787 × 10^{-3} (7.12)	180	Un
3	1.8842 × 10^{-4} (2.37)	1.9072 × 10^{-3} (6.23)	100	Un
4	5.5298 × 10^{-4} (3.81)	1.8176 × 10^{-3} (7.15)	290 × 70	Al-rich silicate
5	4.2780 × 10^{-4} (1.65)	2.3402 × 10^{-3} (3.97)	600	GEMS
6	5.3377 × 10^{-4} (2.77)	1.8902 × 10^{-3} (5.35)	200	Un
7	4.5510 × 10^{-4} (1.95)	2.2892 × 10^{-3} (4.49)	360	Orthopyroxene
8	9.5447 × 10^{-4} (6.73)	1.7168 × 10^{-3} (10.2)	210	Olivine
9	4.4985 × 10^{-4} (2.83)	1.6832 × 10^{-3} (7.53)	350	Olivine

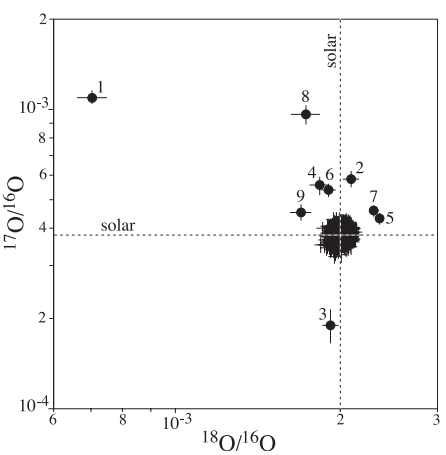

Fig. 2. Oxygen isotopic compositions of nine anomalous silicate grains from Acfer 094 along with the range for grains of normal isotopic composition, which cluster around the solar composition. Errors are given as 1σ. The numbers correspond to those in Table 1. The compositions of the presolar candidates fall outside the range for other matrix grains in the meteorite. The dashed lines indicate the solar ratios for ^{17}O/^{16}O (0.000383) and ^{18}O/^{16}O (0.002005).

dance of presolar silicate grains was calculated to be ~40 ppm relative to the matrix fraction and ~25 ppm relative to the whole meteorite. This abundance is higher than those of other presolar grains in meteorites, with the possible exception of nanodiamonds (*20*).

Isotopic analysis of several elements in presolar grains has previously been restricted mostly to carbonaceous phases (SiC and graphite). Presolar silicates provide an opportunity to explore the isotopic compositions of Si in addition to other major elements (O, Mg, and possibly Ca and Fe if it is inherent to the grain) in grains that originate from O-rich stars. These isotopic ratios are affected by different nucleosynthetic processes occurring at different stages of stellar evolution, which, in AGB stars, must have occurred before they turned into carbon stars. In low- to intermediate-mass stars, the stars identified as the sources of the large majority of O-rich presolar grains, including those of the present study, ^{17}O is enriched and ^{18}O is depleted by H-burning during the main-sequence phase, followed by the first and second dredge-up during the red giant branch (RGB) phase that brings processed material into the star's envelope, where grains eventually form (*21*). Oxygen is also affected by extra mixing processes ("cool bottom processing" or CBP) during which material from the envelope is cycled to regions hot enough for H-burning (*22*, *23*) and by "hot bottom burning" (HBB) during which the convective envelope extends into the H-burning shell (*24*, *25*). These processes occur during the RGB or AGB phases. Aluminum-26 is produced from ^{25}Mg by H-burning in the H-burning shell during the AGB phase and is brought to the stellar surface during third dredge-up episodes associated with thermal pulses but also by CBP and HBB (*26*–*28*). Thermal pulses occur in the thermally pulsing AGB phase when the H-burning shell deposits enough He onto an inactive He-shell to periodically ignite it. Magnesium, Si, and Ca are affected by neutron capture in the He-intershell, which is the He- and C-rich region between the H- and He-burning shells, and in thermal pulses during Heburning (*29*). In addition, the isotopic ratios of all elements reflect the original isotopic composition of the parent star.

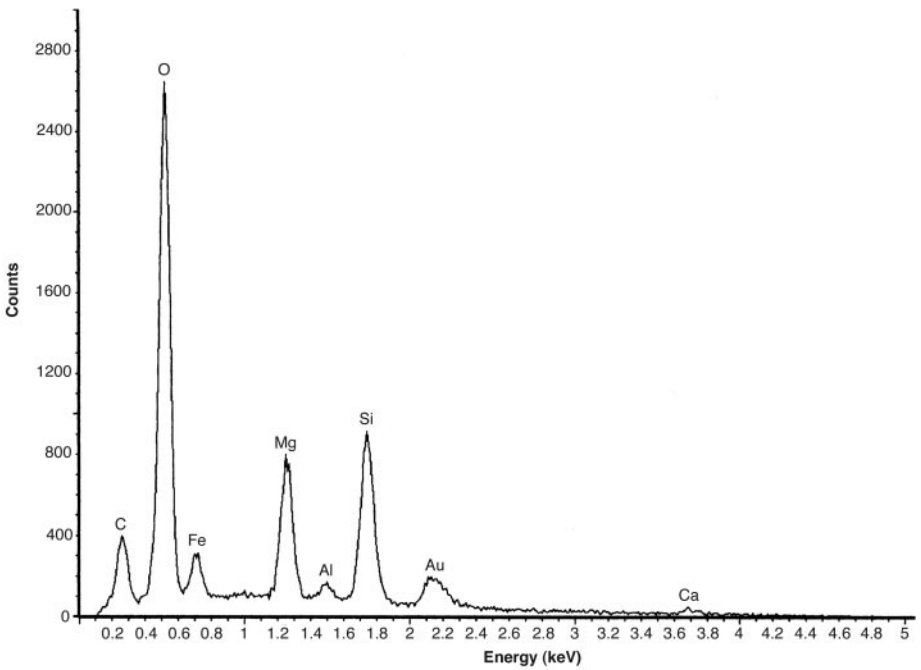

Fig. 3. EDX spectrum of presolar grain #1 obtained with an electron energy of 5 keV to limit contributions from adjacent grains. The presence of Ca suggests that this grain is a clinopyroxene. Although this grain is 500 nm in size, we still obtained a Au signal from the Au substrate; the C signal is from contamination in the SEM.

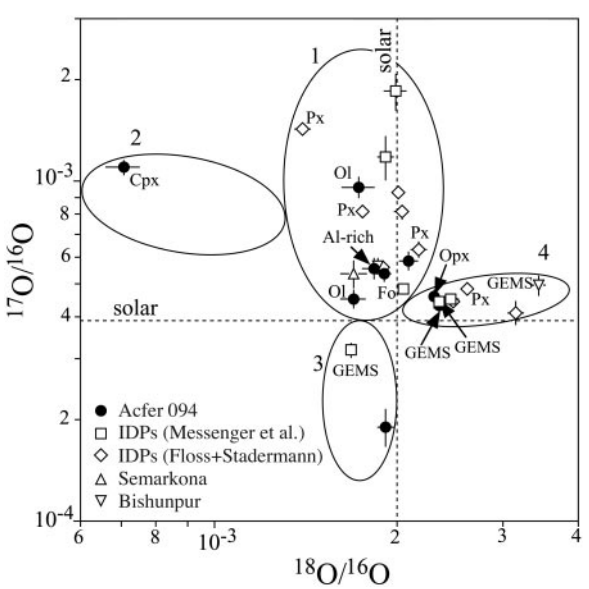

Fig. 4. Oxygen isotopic compositions of presolar silicate grains from Acfer 094 are compared with those of silicates from various IDPs (*11*, *12*) and from the ordinary chondrites Semarkona and Bishunpur (*14*, *15*). Errors are 1σ. The mineralogy of the grains is indicated. Clinopyroxene, Cpx; orthopyroxene, Opx; olivine, Ol; pyroxene, Px; forsterite, Fo. Also shown are the four different groups of grains defined by Nittler *et al*. (*30*).

We compared the O isotopic composition of presolar silicate grains found in Acfer 094 to those found in ordinary chondrites (*14*, *15*) and in IDPs (*11*, *12*) (Fig. 4), but due to limited statistics we cannot make any compositional distinctions. Presolar corundum (Al_2O_3) and spinel ($MgAl_2O_4$) grains have been classified into four groups according to their O isotopic compositions (*30*). Group 1 grains have slight depletions in ^{18}O and are enriched in ^{17}O, which is attributed to the first and second dredge-up phases of stellar evolution. Five of the nine presolar silicates in our study belong to this group. Group 2 grains, produced in low-mass stars, are less enriched in ^{17}O but are distinguished by their large depletion in ^{18}O, explained to be the result of CBP (*22*). Although none of the circumstellar silicates found in IDPs fall into this group, grain #1 from this study has a large ^{18}O depletion. The effects of galactic evolution on the O isotopic ratios of the grains' parent stars (*31*) are reflected in ^{16}O-rich Group 3 grains, believed to have formed in low-metallicity stars. Grain #3 shows this isotopic signature. Group 4 grains with moderate ^{17}O and ^{18}O enrichments point to high-metallicity parent stars, but those grains with the highest enrichments could have been produced in supernovae (*32*). We have found two grains that belong to this group. Presolar silicate grains identified so far span all four groups, with most of them originating from low-mass RGB and AGB stars.

So far, neither the Mg nor the Si isotopic compositions of silicates in IDPs have been determined. We have measured the Mg isotopes in the Group 2 presolar silicate from Acfer 094 and found it to be enriched in ^{26}Mg. This excess ^{26}Mg is most likely due to the in situ decay of the short-lived radionuclide ^{26}Al (half life = 0.7 million years). The $^{27}Al/^{24}Mg$ ratio of the grain was obtained by EDX analysis (Fig. 3), and the inferred initial $^{26}Al/^{27}Al$ of

~0.12 for this grain is higher than any reported to date in presolar oxide grains (*30*, *33*, *34*). However, shell H-burning and third dredge-up in low-mass AGB stars produce a $^{26}Al/^{27}Al$ ratio of only $\sim 1.5 \times 10^{-3}$ in the envelope (*26*). Another consideration is that the grain has to form before dredge-up of C turns the star into a carbon star (*23*). Consequently, another process must be invoked to account for the large $^{26}Al/^{27}Al$. Previously, CBP was invoked to account for the high $^{26}Al/^{27}Al$ ratios found in a corundum and a hibonite grain (*34*). As mentioned already, CBP occurs in low-mass stars during the RGB and the thermally pulsing AGB phases. Although CBP alters the O and Al isotopic abundances simultaneously, there is no correlation between the two systems because the decrease in $^{18}O/^{16}O$ is dependent on the rate of mass circulation ($\dot{M}$), whereas $^{26}Al/^{27}Al$ depends on the maximum temperature of the circulated material (T_P), which in turn depends on depth of penetration (*23*). According to CBP models for a 1.5 $M_\odot$ (solar mass) star (*23*), ^{26}Al is abundantly produced for $\log T_P > 7.65$, but the large $^{26}Al/^{27}Al$ observed in the presolar silicate grain requires $\log T_P > 7.76$ and very deep mixing. In addition, the O isotopic composition of this grain requires $\dot{M} > 10^{-6}\ M_\odot$ per year. These values for T_P and $\dot{M}$ are feasible in low-mass thermally pulsing AGB stars undergoing CBP. It is apparent that the combined isotopic analysis of O and Mg provides more detailed information on deep mixing processes than just one isotopic system would provide.

In combining the data for all presolar silicates in IDPs (*11*, *12*), we arrive at a total abundance of ~890 ppm (*9*). In contrast, the abundance in Acfer 094 relative to the matrix material is ~40 ppm. This difference confirms that IDPs are more primitive than any meteorite. The abundance of circumstellar silicates in the matrix of the ordinary chondrites Semarkona and Bishunpur has been inferred to be ~15 ppm (*14*, *15*) compared with ~40 ppm in Acfer 094. These ordinary chondrites have undergone more aqueous alteration than Acfer 094 and formed at higher temperatures. This difference in abundance gives us a first look at the effects of meteorite formation histories and parent body processes on presolar grain survival. Determination of the abundances of presolar silicates in other meteorite classes will give us a means of studying the physical conditions in different solar system environments. Due to the unusually primitive nature of Acfer 094, we do not expect the abundance to be higher in other meteorites, but we still do not understand the destructive processes affecting presolar silicate grains well enough to make this a firm prediction.

References and Notes

1. E. Zinner, in *Meteorites, Comets, and Planets*, A. M. Davis, Ed. (Elsevier, Oxford, UK, 2004), vol. 1, pp. 17–39.
2. C. Waelkens *et al.*, *Astron. Astrophys.* **315**, L245 (1996).
3. K. Malfait *et al.*, *Astron. Astrophys.* **332**, L25 (1998).
4. L. B. F. M. Waters *et al.*, *Astron. Astrophys.* **315**, L361 (1996).
5. K. Demyk, E. Dartois, H. Wiesemeyer, A. P. Jones, L. d'Hendecourt, *Astron. Astrophys.* **364**, 170 (2000).
6. L. R. Nittler, thesis, Washington University (1996).
7. S. Messenger, T. J. Bernatowicz, *Meteorit. Planet. Sci.* **35**, A109 (2000).
8. C. M. O'D. Alexander, L. Nittler, F. Tera, *Lunar Planet. Sci.* **XXXII**, A2191 (2001).
9. Materials and methods are available as supporting material on *Science* Online.
10. A. Nguyen, E. Zinner, R. S. Lewis, *Publ. Astron. Soc. Aust.* **20**, 382 (2003).
11. S. Messenger, L. P. Keller, F. J. Stadermann, R. M. Walker, E. Zinner, *Science* **300**, 105 (2003).
12. C. Floss, F. J. Stadermann, *Lunar Planet. Sci.* **XXXV**, A1281 (2004).
13. J. P. Bradley, *Science* **265**, 925 (1994).
14. S. Mostefaoui, P. Hoppe, K. K. Marhas, E. Gröner, *Meteorit. Planet. Sci.* **38**, A99 (2003).
15. S. Mostefaoui, K. K. Marhas, P. Hoppe, *Lunar Planet. Sci.* **XXXV**, A1593 (2004).
16. F. J. Molster, L. B. F. M. Waters, A. G. G. M. Tielens, C. Koike, H. Chihara, *Astron. Astrophys.* **382**, 241 (2002).
17. F. J. Molster *et al.*, *Nature* **401**, 563 (1999).
18. S. Weinbruch, H. Palme, W. F. Müller, A. El Goresy, *Meteoritics* **25**, 115 (1990).
19. X. Hua, J. Adam, A. El Goresy, H. Palme, *Geochim. Cosmochim. Acta* **52**, 1389 (1988).
20. E. Zinner, *Annu. Rev. Earth Planet. Sci.* **26**, 147 (1998).
21. A. I. Boothroyd, I.-J. Sackmann, *Astrophys. J.* **510**, 232 (1999).
22. G. J. Wasserburg, A. I. Boothroyd, I.-J. Sackmann, *Astrophys. J.* **447**, L37 (1995).
23. K. M. Nollett, M. Busso, G. J. Wasserburg, *Astrophys. J.* **582**, 1036 (2003).
24. A. I. Boothroyd, I.-J. Sackmann, G. J. Wasserburg, *Astrophys. J.* **442**, L21 (1995).
25. R. C. Cannon, C. A. Frost, J. C. Lattanzio, P. R. Wood, in *Nuclei in the Cosmos III*, M. Busso, R. Gallino, C. M. Raiteri, Eds. (AIP, New York, 1995), pp. 469–472.
26. M. Forestini, G. Paulus, M. Arnould, *Astron. Astrophys.* **252**, 597 (1991).
27. N. Mowlavi, G. Meynet, *Astron. Astrophys.* **361**, 959 (2000).
28. A. I. Karakas, J. C. Lattanzio, *Publ. Astron. Soc. Aust.* **20**, 279 (2003).
29. M. Busso, R. Gallino, G. J. Wasserburg, *Annu. Rev. Astron. Astrophys.* **37**, 239 (1999).
30. L. R. Nittler, C. M. O'D. Alexander, X. Gao, R. M. Walker, E. Zinner, *Astrophys. J.* **483**, 475 (1997).
31. C. M. O'D. Alexander, L. R. Nittler, *Astrophys. J.* **519**, 222 (1999).
32. B.-G. Choi, G. R. Huss, G. J. Wasserburg, R. Gallino, *Science* **282**, 1284 (1998).
33. I. D. Hutcheon, G. R. Huss, A. J. Fahey, G. J. Wasserburg, *Astrophys. J.* **425**, L97 (1994).
34. B.-G. Choi, G. J. Wasserburg, G. R. Huss, *Astrophys. J.* **522**, L133 (1999).

35. We thank the reviewer for valuable comments and are grateful to S. Amari and C. Floss for their assistance with SEM measurements and helpful discussions. We also thank S. Messenger and F. Stadermann for developing the software for processing the isotopic images. Supported by NASA grants NAG5-10426 and NAG5-11545.

Supporting Online Material

www.sciencemag.org/cgi/content/full/303/5663/1496/DC1
Materials and Methods
Table S1
References

5 December 2003; accepted 30 January 2004

European Seasonal and Annual Temperature Variability, Trends, and Extremes Since 1500

Jürg Luterbacher,[1,2]* Daniel Dietrich,[3] Elena Xoplaki,[2] Martin Grosjean,[1] Heinz Wanner[1,2]

Multiproxy reconstructions of monthly and seasonal surface temperature fields for Europe back to 1500 show that the late 20th- and early 21st-century European climate is very likely (>95% confidence level) warmer than that of any time during the past 500 years. This agrees with findings for the entire Northern Hemisphere. European winter average temperatures during the period 1500 to 1900 were reduced by ~0.5°C (0.25°C for annual mean temperatures) compared to the 20th century. Summer temperatures did not experience systematic century-scale cooling relative to present conditions. The coldest European winter was 1708/1709; 2003 was by far the hottest summer.

Detailed insight into high-resolution temporal and spatial patterns of climate change during previous centuries is essential for assessing the degree to which late 20th-century changes may be unusual in the light of preindustrial natural climate variability (*1–3*). Climate change at seasonal to annual resolutions for recent centuries has been highlighted in a number of studies, which have included climate modeling experiments with estimated natural and anthropogenic radiative-forcing changes (*4–6*) and empirical hemispheric or global reconstructions. Such reconstructions are based either on natural archives only (such as ice cores, tree rings, speleothems, varved sediments, and subsurface temperature profiles obtained from borehole measurements) or on multiproxy networks that amalgamate natural proxy indicators with climate information obtained from early instrumental and documentary evidence (*7–14*). A number of these reconstructions support the conclusion that the warmth of the late 20th century is likely unprecedented in the Northern

[1]National Center of Competence in Research (NCCR) Climate, [2]Institute of Geography, Climatology, and Meteorology, [3]Department of Mathematical Statistics and Actuarial Science, University of Bern, CH–3012 Bern, Switzerland.

*To whom correspondence should be addressed. E-mail: juerg@giub.unibe.ch